CHAPTER 3

RESULTS AND DISCUSSION

3.1 Pure CeO_2 nanoparticles and Ag-doped CeO_2 nanoparticles Characterization

In this research, pure CeO_2 nanoparticles and Ag-doped CeO_2 nanoparticles were characterized by X-ray diffraction (XRD), Scanning Electron Microscopy (SEM), energy-dispersive X-ray spectrometry (EDS), Transmission Electron Microscopy (TEM) and Brunauer-Emmett-Teller (BET) analysis.

3.1.1 Thermogravimetric analysis (TG) and Differential scanning calorimetry (DSC)

The TG/DTA spectrum in Figure 3.1 shows the thermal decomposition process for the cerium(IV) hydroxide. The total measured weight loss from 25 to 1,000^{o}C was 17.92%, according with the theoretical weight loss for the decomposition of cerium hydrate oxide, i.e. $Ce(OH)_3$ to CeO_2. As temperature increased to 500^{o}C, the $Ce(OH)_3$ decomposed endothermally to produce the final product, CeO_2 suggesting that the complete formation on CeO_2 occurs after 500^{o}C.

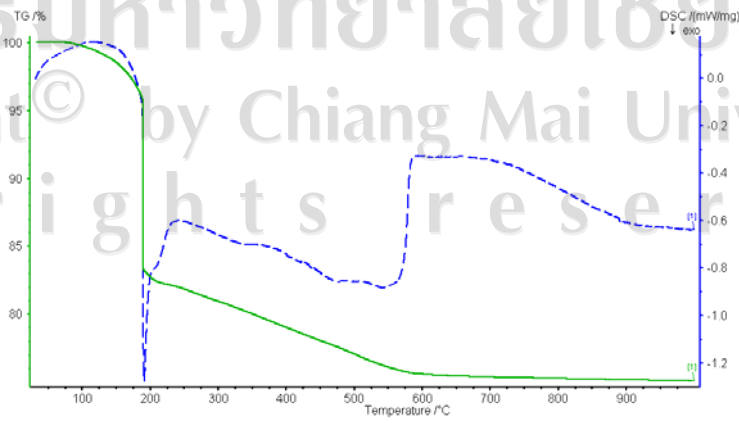

Figure 3.1 Thermal decomposition process for the cerium(IV) hydroxide.

The TG/DTA spectrum in Figure 3.2 shows the thermal decomposition process for pure CeO_2 nanoparticles with difference Ag doping levels. As temperature increased to 400°C, the samples decomposed to produce the final product, suggesting that the complete formation on Ag/CeO_2 occurs after 400°C.

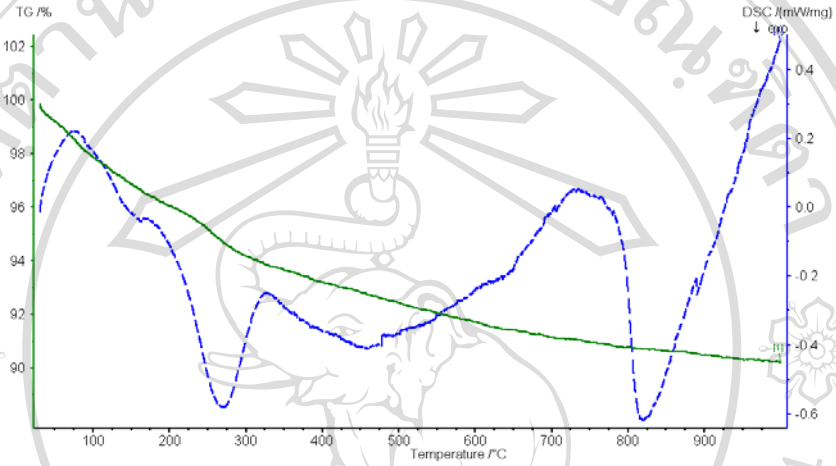

Figure 3.2 Thermal decomposition process for pure CeO_2 nanoparticles with difference silver doping levels

3.1.2 X-ray diffraction analysis (XRD)

The crystallinity of the synthesized samples was examined by XRD analysis. XRD patterns of pure CeO_2 nanoparticles and 0.10, 0.25, 0.50, 0.75 and 1.00mol% Ag-doped CeO_2 nanoparticles synthesized by the homogeneous precipitation method and the impregnation method, respectively, were shown in Figure 3.3. The accurate evaluation of the position of the main reflections of CeO_2 corresponding to the (111), (200), (220), (311), (222) and (400) accordance with the data in the JCPDS card no.34-394 of a cubic phase CeO_2. The sharper and broader peaks of diffraction patterns were indicated to be the bigger particles and smaller particles, respectively. It was observed that the XRD patterns showed no signals originated the presence of

doped metal sample, it's mean as a comparison doping Ag-doped CeO_2 nanoparticles with absence of Ag loading, the peaks of diffraction pattern and intensity were not seen in the different because the low dosage of silver content.

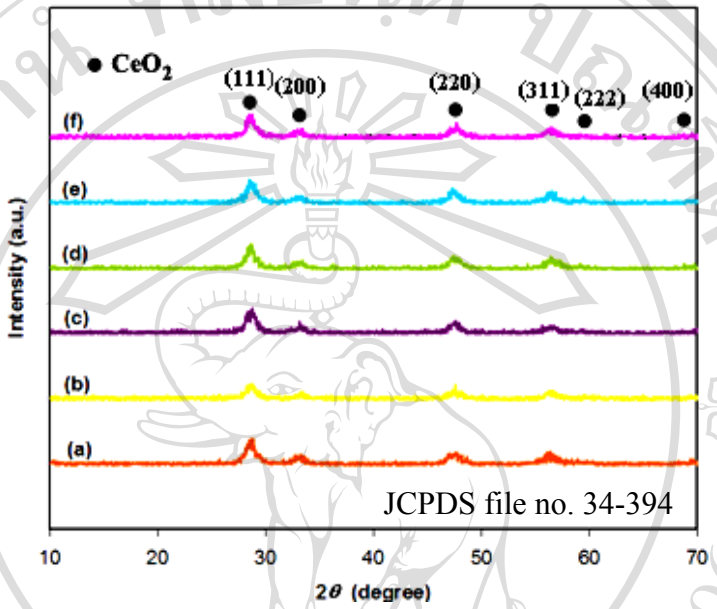

Figure 3.3 X-ray diffraction patterns of (a) pure CeO_2, (b) 0.10mol% Ag/CeO_2, (c) 0.25mol% Ag/CeO_2 , (d) 0.50mol% Ag/CeO_2 , (e) 0.75mol% Ag/CeO_2 and (f) 1.00mol% Ag/CeO_2

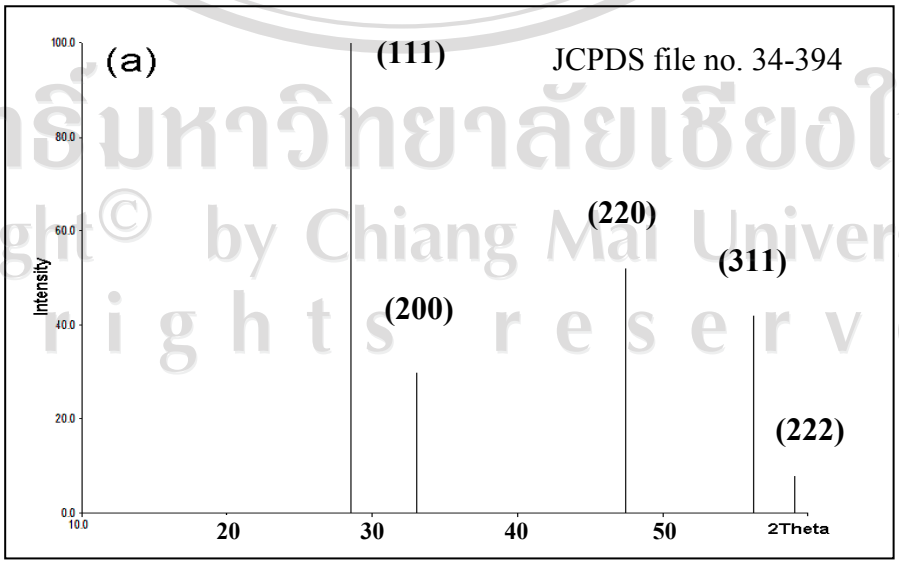

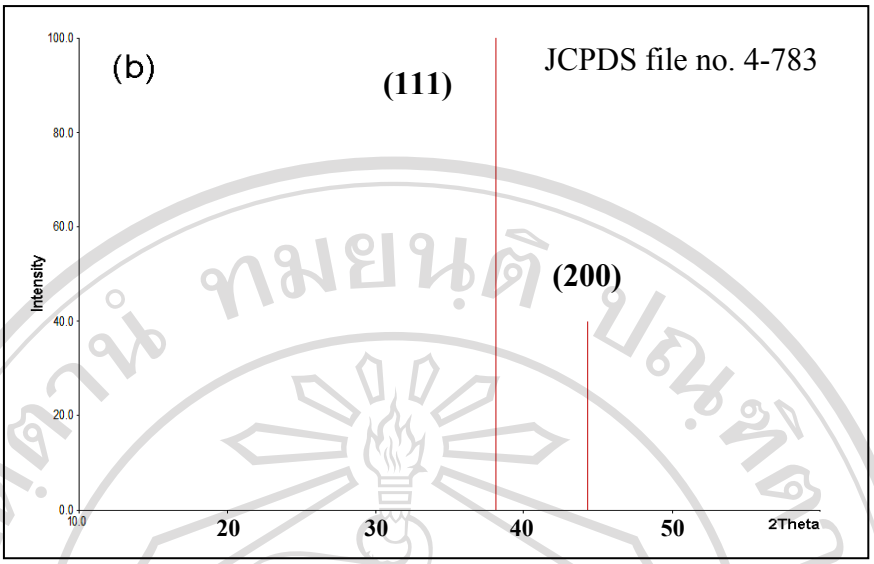

Figure 3.4 (a) JCPDS file no. 34-394 of cubic phase structure of CeO_2 and (b) JCPDS file no. 4-783 of cubic phase structure of Ag

3.1.3 Scanning Electron Microscopy (SEM) and energy-dispersive X-ray spectrometry (EDS)

The SEM image and EDS mapping mode of pure CeO_2 nanoparticles and 0.10, 0.25, 0.50, 0.75 and 1.00mol% Ag-doped CeO_2 nanoparticles were shown in Figure 3.5 and 3.6, illustrates the SEM micrographs clearly showed the surface morphology nanostructural of CeO_2 nanoparticles was nearly spherical in shape and dispersing well as shown in Figure 3.5. The particle sizes of pure CeO_2 nanoparticles and 0.10, 0.25, 0.50, 0.75 and 1.00mol% Ag-doped CeO_2 nanoparticles were found to be in the same range of 15-20 nm in diameter. Figures 3.6 shows the chemical compositions of pure CeO_2 nanoparticles and 0.10, 0.25, 0.50, 0.75 and 1.00mol% Ag-doped CeO_2 nanoparticles were analyzed from EDS spectra. The element compositions data from EDS confirmed silver was actually in Ag-doped CeO_2 nanoparticles because appearence of the signal of EDS spectrum corresponded to Ag,

Ce and O elements. However, the amount of element composition was slightly different depending on the different selected focus area of EDS analysis.

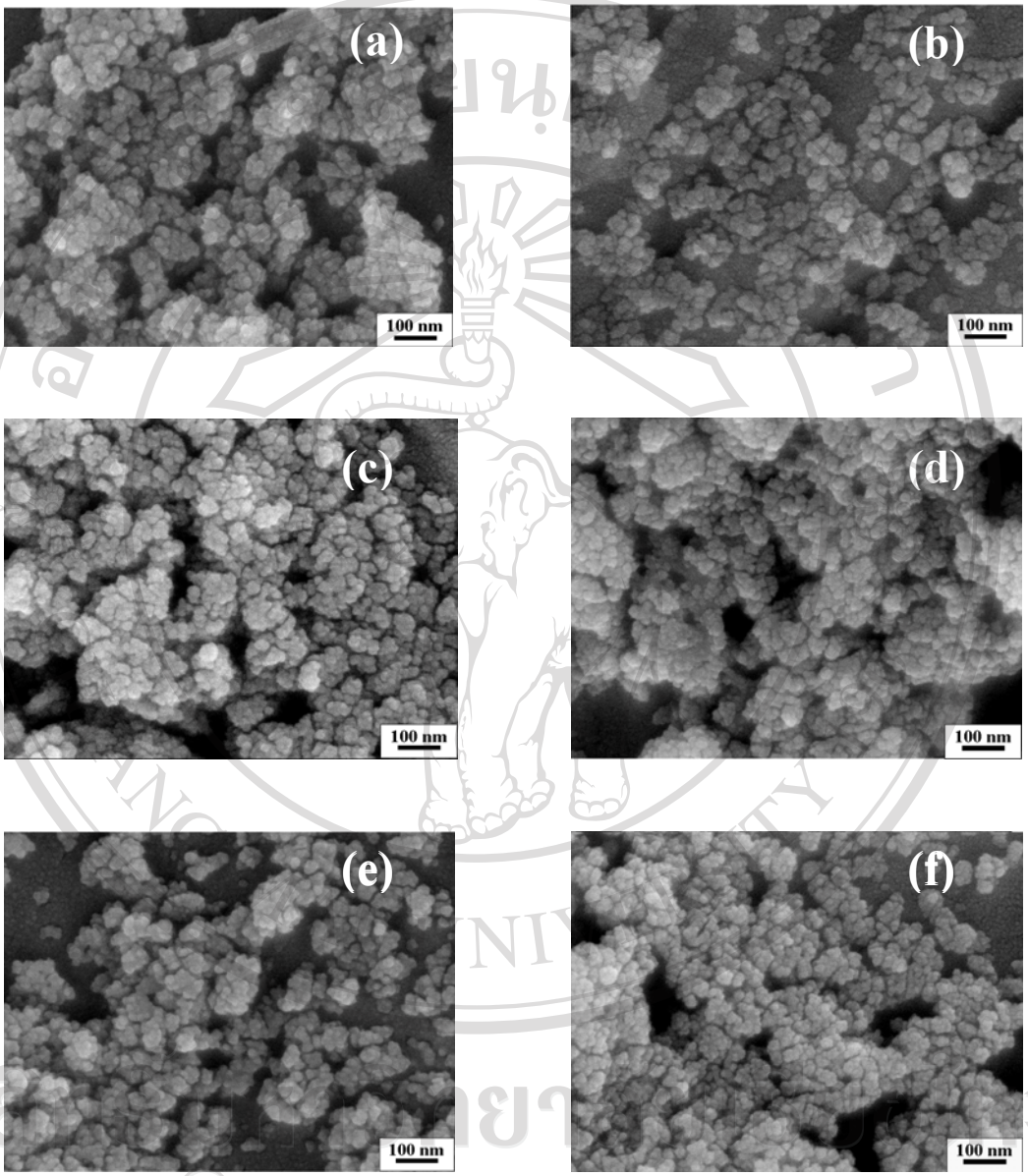

Figure 3.5 SEM images of (a) pure CeO_2, (b) 0.10 mol% of Ag/CeO_2, (c) 0.25 mol% of Ag/CeO_2, (d) 0.50 mol% of Ag/CeO_2, (e) 0.75 mol% of Ag/CeO_2 and (f) 1.00 mol% of Ag/CeO_2

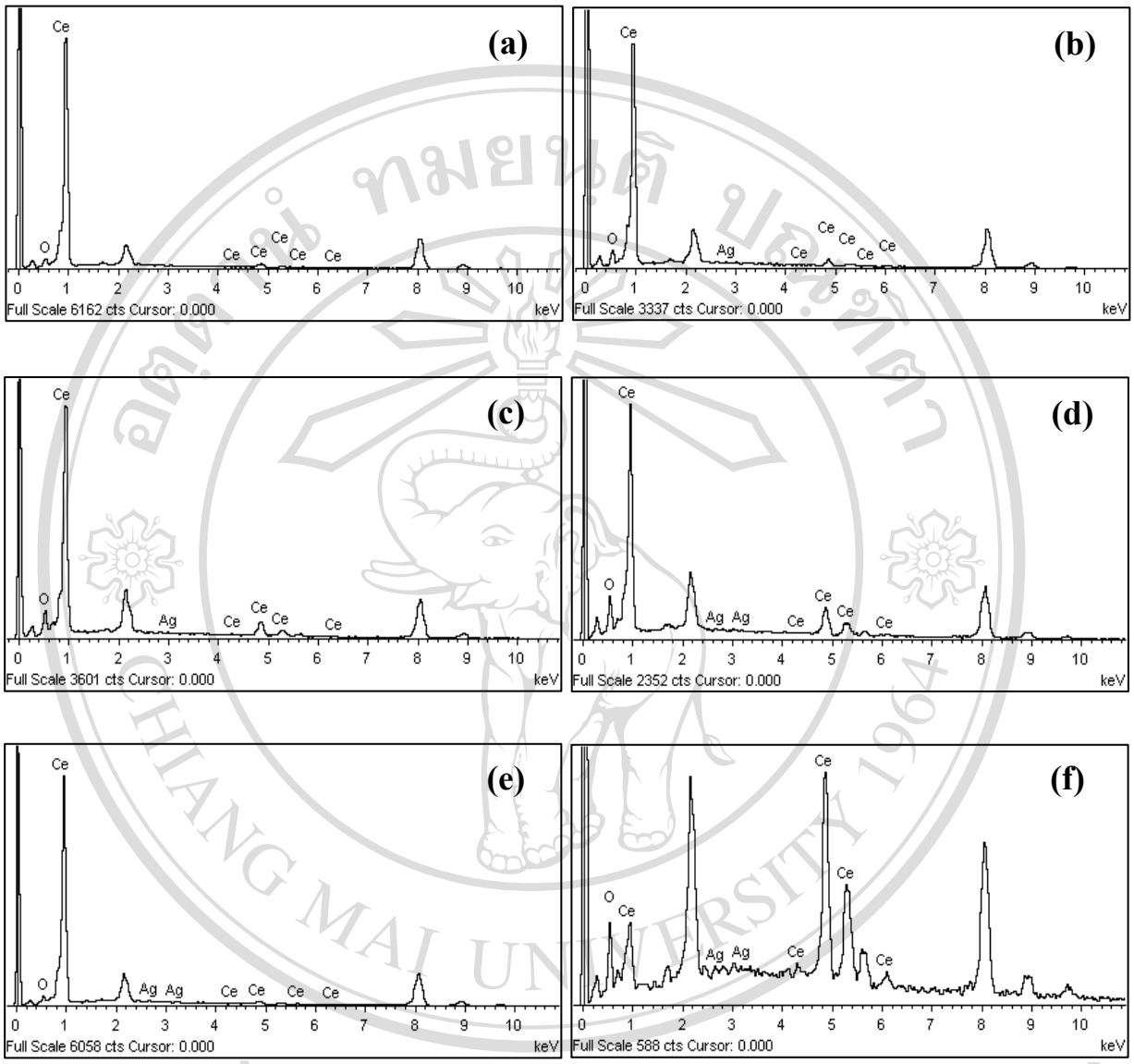

Figure 3.6 EDS analysis of (a) pure CeO_2, (b) 0.10 mol% of Ag/CeO_2, (c) 0.25 mol% of Ag/CeO_2, (d) 0.50 mol% of Ag/CeO_2, (e) 0.75 mol% of Ag/CeO_2 and (f) 1.00 mol% of Ag/CeO_2

3.1.4 Transmission Electron Microscopy (TEM)

The accurate sizes of pure CeO_2 nanoparticles and Ag-doped CeO_2 nanoparticles were clearly confirmed by TEM images. Figure 3.7 (a), (b), (c), (d), (e) and (f) shown the TEM images of pure CeO_2 nanoparticles and 0.10, 0.25, 0.50, 0.75 and 1.00 mol% of Ag-doped CeO_2 nanoparticles, respectively. For the pure CeO_2 nanoparticles shown in Figure 3.7 (a), it can be found that the crystallite size was about 5–6 nm. The particles are not well-defined due to its small size. To further observe, for the 0.10-1.00mol% of Ag-doped CeO_2 shown in Figure 3.7 (b-f), particles were very well defined and relatively dispersed. Good crystalline faces and crystallinity state could be observed. The crystallite size was about 7–8 nm. The particle size was found to become bigger in the presence of silver metal.

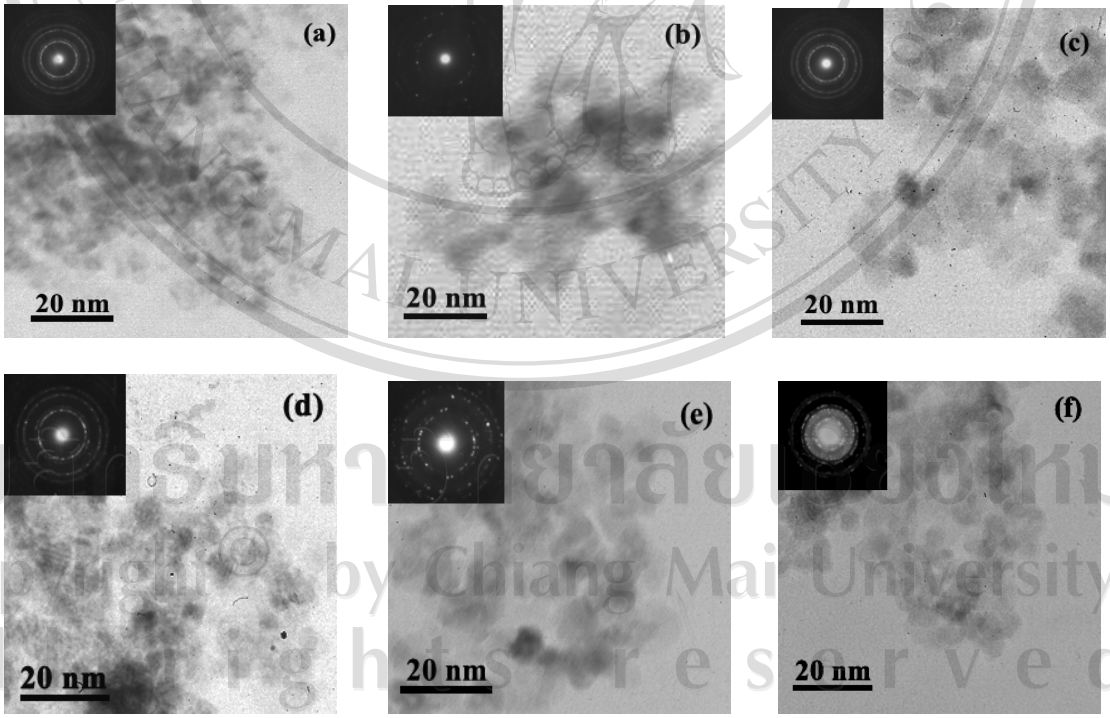

Figure 3.7 TEM images of (a) pure CeO_2, (b) 0.10 mol% of Ag/CeO_2, (c) 0.25 mol% of Ag/CeO_2, (d) 0.50 mol% of Ag/CeO_2, (e) 0.75 mol% of Ag/CeO_2 and (f) 1.00 mol% of Ag/CeO_2

3.1.5 Brunauer-Emmett-Teller (BET) analysis

The specific surface area of pure CeO_2 nanoparticles and 0.10, 0.25, 0.50, 0.75 and 1.00 mol% of Ag-doped CeO_2 nanoparticles were measured by nitrogen adsorption after degassing the sample at 150ºC were 109.40, 82.37, 110.80, 77.99, 114.47 and 96.93 m^2/g, corresponded to BET equivalent diameter of 7.2, 9.5, 7.1, 10.0, 6.8 and 8.1 nm, respectively as shown in Table 3.1. Figure 3.7 shows the comparison of SSA and d_{BET} of pure CeO_2 and 0.10, 0.25, 0.50, 0.75 and 1.00 mol% of Ag-doped CeO_2 nanoparticles. From these data, it can be clearly seen that the particles size calculated by BET measurement using SSA_{BET} and the density of CeO_2 (ρ_{CeO_2} = 7.65 g/cm^3) was the same value. The specific area of pure CeO_2 nanoparticles and Ag-doped CeO_2 nanoparticles that calculated the result of SSA by BET were found to be in the range of 6-10 nm, it can be summarize that as the amount of silver metal loading did not have effect to the particles size of CeO_2.

Table 3.1 SSA and BET equivalent diameter of pure CeO_2 nanoparticles and 0.10-1.00 mol% of Ag-doped CeO_2 nanoparticles

Samples	SSA(m^2/g)	dBET (nm)
pure CeO_2	109.40	7.2
0.10 mol% Ag-doped CeO_2	82.37	9.5
0.25 mol% Ag-doped CeO_2	110.80	7.1
0.50 mol% Ag-doped CeO_2	77.99	10.0
0.75 mol% Ag-doped CeO_2	114.47	6.8
1.00 mol% Ag-doped CeO_2	96.93	8.1

3.2 Photocatalytic activity measurement

The photocatalytic activity of pure CeO_2 nanoparticles and Ag-doped CeO_2 nanoparticles were investigated for the degradation of oxalic acid and formic acid under UVA-light irradiation.

3.2.1 Calibration curve

The conductivity probe was used to detect the amount of carbon generated in the spiral photoreactor. The probe was calibrated by mineralizing at different concentrations of oxalic acid. The calibration data from conductivity reading at different concentrations of carbon in microgram was plotted in natural logarithmic scale as shown in Figure 3.8. Table 3.2 shows the calibration data of different concentration of oxalic acid.

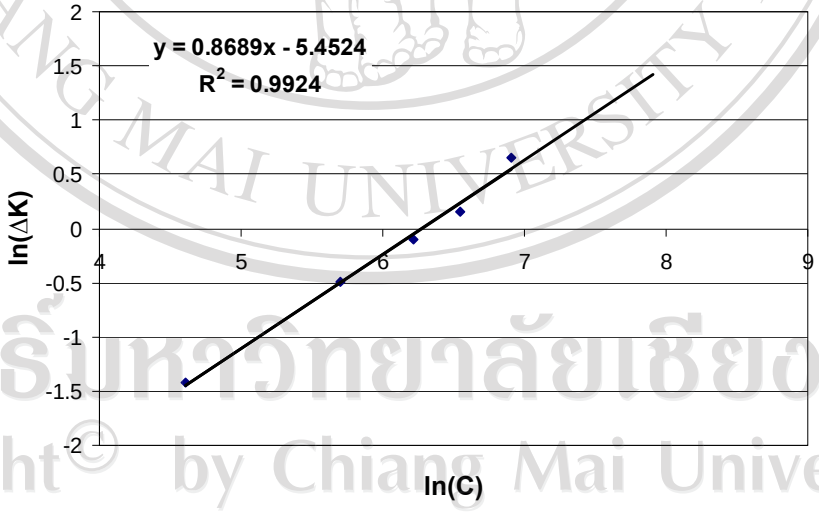

Figure 3.8 Calibration slope for conductivity probe

Table 3.2 Calibration data of different concentrations of oxalic acid

Amount of carbon (µg)	ln C	conductivity (k, µS/cm) (initial value k=5.39)	Δk	Ln (Δk)	Injection volume (µL)	Cumulative volume (µL)
100	4.6051	5.63	0.24	-1.4271	20	20
300	5.7038	6.00	0.61	-0.4943	40	60
500	6.2146	6.30	0.85	-0.0943	40	100
700	6.5511	6.56	1.17	0.1570	40	140
1000	6.9078	7.30	1.91	0.6471	60	200

The plot of ln(C) value with ln(ΔK) value was showed the linear relationship, respond which the equation of ln(ΔK)=0.8689 ln(C) –5.4524 and R-squared = 0.9924. It can be confirmed that the calibration curve was high accuracy because the number of R-squared about one. The linear equation of calibration curve was converted to the mass of CO_2 generated for degradation of organic compound.

3.2.2 Photocatalytic activity of pure CeO_2 nanoparticles and Ag-doped CeO_2 nanoparticles with oxalic acid

The rate of 50% mineralization of oxalic acid with 500 µg of carbon by using pure CeO_2 nanoparticles and 0.10, 0.25, 0.50, 0.75 and 1.00 mol% of Ag-doped CeO_2 nanoparticles under UVA-light irradiation as shown in Figure 3.9. The photocatalytic activity of pure CeO_2 nanoparticles was higher than Ag-doped CeO_2 nanoparticles. In the part of the mineralization of oxalic acid was up and down, using 0.50mol% of Ag-doped CeO_2 nanoparticles showed the highest activity mineralized oxalic acid under UVA-light irradiation.

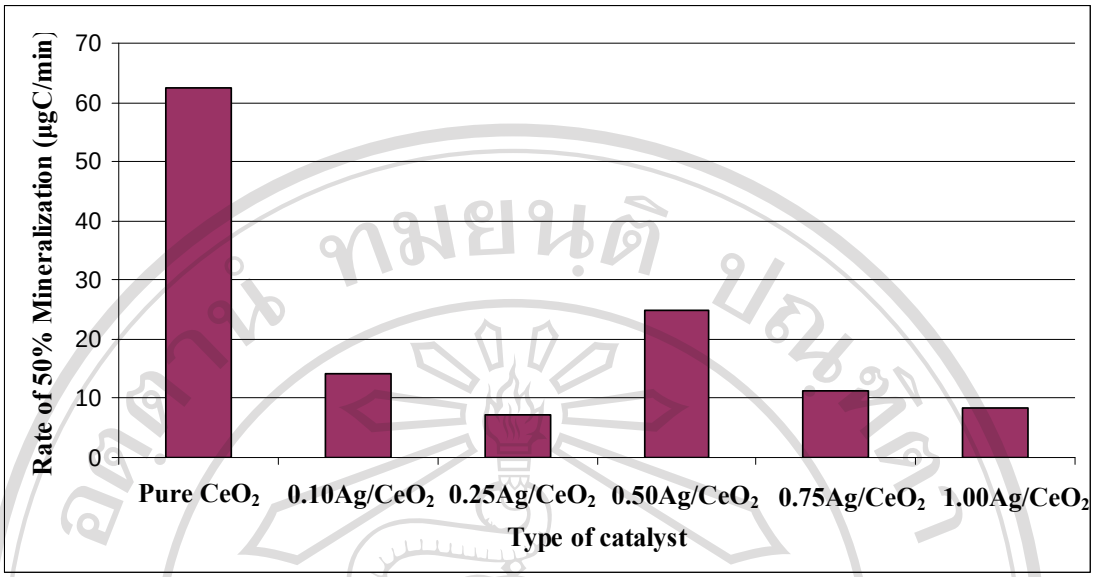

Figure 3.9 The rate of 50% mineralization of oxalic acid with 500 µg of carbon by using pure CeO_2 nanoparticles and 0.10-1.00 mol% of Ag-doped CeO_2 nanoparticles under UVA-light irradiation

3.2.3 Photocatalytic activity of pure CeO_2 nanoparticles and Ag-doped CeO_2 nanoparticles with formic acid

The rate of 50% mineralization of formic acid with 500 µg of carbon by using pure CeO_2 nanoparticles and 0.10, 0.25, 0.50, 0.75 and 1.00 mol% of Ag-doped CeO_2 nanoparticles under UVA-light irradiation as shown in Figure 3.10. The photocatalytic activity of pure CeO_2 nanoparticles was higher than Ag-doped CeO_2 nanoparticles. In the part of the mineralization of formic acid using Ag-doped CeO_2 nanoparticles, the initial was decreased until to 0.50mol% of Ag-doped CeO_2 nanoparticles, rate was increased and decreasing when used 1.00mol% of Ag-doped CeO_2 nanoparticles. It was found that the mineralization of formic acid using 0.75mol% of Ag-doped CeO_2 nanoparticles showed the highest activity mineralized formic acid under UVA-light irradiation.

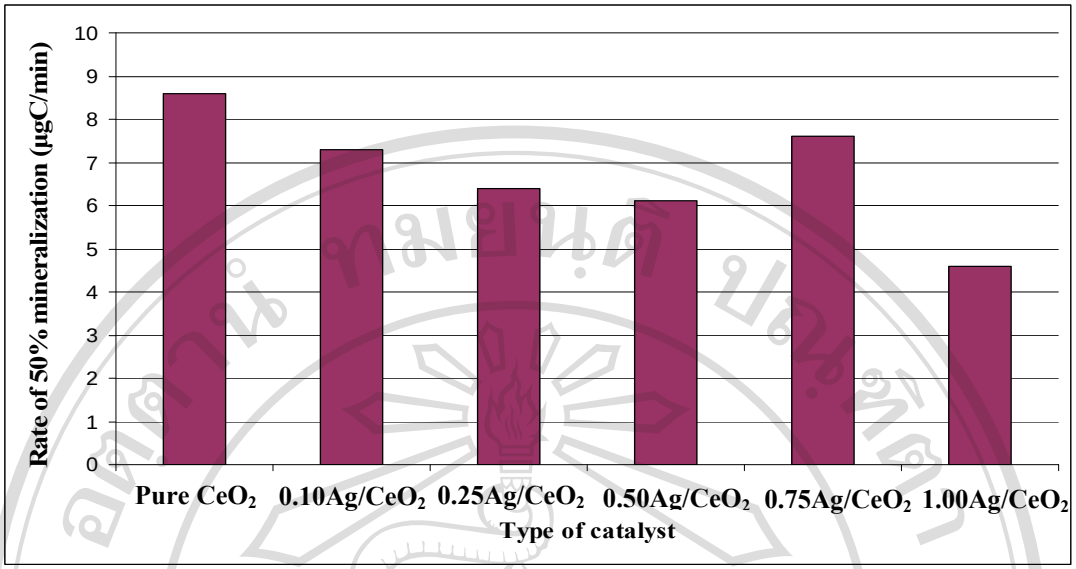

Figure 3.10 The rate of 50% mineralization of formic acid with 500 µg of carbon by using pure CeO_2 nanoparticles and 0.10-1.00 mol% of Ag-doped CeO_2 nanoparticles under UVA-light irradiation

Table 3.3 Time of 50% mineralization of organic compound with 500 µg of carbon by using pure CeO_2 nanoparticles and 0.10-1.00 mol% of Ag-doped CeO_2 nanoparticles under UVA-light irradiation

Type of catalyst	**Time of 50% mineralization (min)**	
	oxalic acid	**formic acid**
Pure CeO_2	4	29
0.10 mol% Ag-doped CeO_2	17.5	34
0.25 mol% Ag-doped CeO_2	35	39
0.50 mol% Ag-doped CeO_2	10	41
0.75 mol% Ag-doped CeO_2	22	33
1.00 mol% Ag-doped CeO_2	30	54

The mineralization times of different organic compounds were compared for various photocatalysts under UVA-light irradiation as shown in Table 3.4. It was also found that pure CeO_2 nanoparticles was more active than Ag-doped CeO_2 nanoparticles. While, the efficiency of Ad-doped CeO_2 nanoparticles for mineralizing of oxalic acid performed better than formic acid because time of 50% mineralization of oxalic acid was less than formic acid. The optimum concentration for silver metal of highest photocatalytic activity for mineralizing oxalic acid and formic acid under UVA-light irradiation were found to be 0.50 and 0.75 mol% Ag-doped CeO_2 nanoparticles, respectively. From this result, it can be concluded that Ag-doped CeO_2 nanoparticles have no effect in improving on photocatalytic activity of pure CeO_2 nanoparticles. The doping of silver ion (Ag^+) to the semiconductor metal oxide (CeO_2) decreased the e^-/h^+ recombination rate. Therefore, the photocatalytic efficiency of Ag-doped CeO_2 nanoparticles was less than pure CeO_2 nanoparticles. In fact, the efficiency of photocatalysts can be explained as the recombination rate of electron/hole pairs and the production rate of reactive free radicals. In general, the use of smaller particle size semiconductor materials can improve the photocatalytic efficiency by increasing electron/hole recombination rate.